RESEARCH ARTICLE SUMMARY

NANOPHOTONICS

A framework for scintillation in nanophotonics

Charles Roques-Carmes*†, Nicholas Rivera*†, Ali Ghorashi, Steven E. Kooi, Yi Yang, Zin Lin, Justin Beroz, Aviram Massuda, Jamison Sloan, Nicolas Romeo, Yang Yu, John D. Joannopoulos, Ido Kaminer, Steven G. Johnson, Marin Soljačić

INTRODUCTION: Bombardment of materials by high-energy particles often leads to light emission in a process known as scintillation. Scintillators, being broadly applicable to the detection of ionizing radiation, have widespread applications, including in x-ray detectors for medical imaging and nondestructive inspection, gamma-ray detectors for positron emission tomography, phosphor screens in night vision systems and electron microscopes, and electromagnetic calorimeters in high-energy physics experiments. Accordingly, there is great interest in the development of "better scintillators" with greater photon yields and improved spatial and energy resolution. Better scintillators in general would lead to definite improvements in all of the above use cases. One example application is medical imaging, where brighter scintillators could enable very-low-dose x-ray imaging, therefore reducing potential harm to patients. Most research into the problem of improving scintillators involves the synthesis of new materials with better intrinsic scintillating properties.

RATIONALE: The conversion of a high-energy particle into photons is a complex, multiphysics process in which the incident particle creates a cascade of secondary electron excitations in the scintillator. These secondary excitations then relax into a non-equilibrium distribution before emitting scintillation photons. By creating spatial inhomogeneities in the scintillator on the scale of the scintillation photon wavelength, and thus modulating the optical properties of the material on the wavelength scale, one can control and enhance the light emission. In such "nanophotonic scintillators," it is then possible for the light-emitting electrons in the scintillator to emit light much more rapidly due to enhancement of the local density of optical states available to the electrons for light emission. It is also possible to use these nanophotonic structures to "steer" trapped light out of the scintillator, enabling more light to be detected. Both of these effects lead to enhanced rates of scintillation photon emission. These nanophotonic effects are material-agnostic, enabling in principle any scintillator to be enhanced, and these effects can also be in principle observed for any type of high-energy particle.

RESULTS: We developed a first-principles theory of nanophotonic scintillators, taking into account the complex processes leading to electron excitation as well as the light emission by non-equilibrium electrons in arbitrary nanophotonic structures. Using the theory as a guide, we experimentally demonstrated order-of-magnitude scintillation enhancements in two different platforms: electron-induced scintillation by silica defects, and x-ray–induced scintillation by rare-earth dopants in conventional scintillators. The enhancements in both cases were enabled by two-dimensionally periodic etching of either the scintillator or the material above the scintillator to create a two-dimensional photonic crystal slab geometry. The theory accounted for the enhancements observed experimentally, as well as other effects that required first-principles description of the underlying microscopic kinetics of the emission process. For example, we could explain the observed spectral shaping as a function of geometrical parameters of the photonic crystal slab. Additionally, using the framework, we could account for nonlinear relationships of the signal on the incident particle flux, as well as effects where the dominant scintillation wavelength could change as a function of high-energy particle flux. Beyond, we used a nanopatterned x-ray scintillator to record x-ray scans of various specimens and observed an increase in image brightness. This directly translates into faster scans, or equivalently a lower x-ray dose required to achieve a given brightness.

CONCLUSION: Our framework can be directly applied to model nanophotonic scintillation in many existing experiments, accounting for arbitrary types of high-energy particles, scintillator materials, and nanophotonic environments. Beyond this, our framework also allows the discovery of optimal nanophotonic structures for enhancing scintillation. We show how topology optimization and other types of nanophotonic structures can be used to find structures that could present even larger scintillation enhancements. We expect that the concept demonstrated here could be deployed in all of the application areas where scintillators are used, with compelling applications throughout, including medical imaging, night vision, and high-energy physics experiments. ■

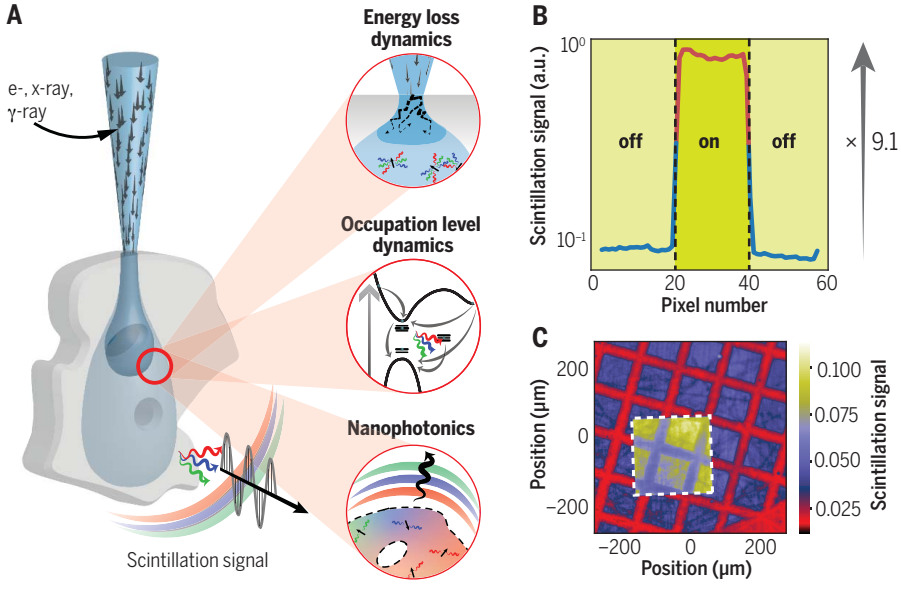

Nanophotonic scintillators. (**A**) Nanophotonic scintillators consist of nanophotonic structures integrated with scintillators. Scintillation can be modeled, tailored, and optimized by combining energy loss dynamics, occupation level dynamics, and nanophotonics modeling. (**B**) Order-of-magnitude x-ray scintillation enhancement with a photonic crystal nanophotonic scintillator. (**C**) X-ray scan taken with a nanophotonic scintillator (white dashed square).

The list of author affiliations is available in the full article online.
*Corresponding author. Email: chrc@mit.edu (C.R.-C.); nrivera@mit.edu (N.R.)
†These authors contributed equally to this work.
Cite this article as C. Roques-Carmes *et al.*, *Science* **375**, eabm9293 (2022). DOI: 10.1126/science.abm9293

READ THE FULL ARTICLE AT
https://doi.org/10.1126/science.abm9293

RESEARCH ARTICLE

NANOPHOTONICS

A framework for scintillation in nanophotonics

Charles Roques-Carmes[1]*†, Nicholas Rivera[2]*†, Ali Ghorashi[2], Steven E. Kooi[3], Yi Yang[1,2,4], Zin Lin[5], Justin Beroz[2], Aviram Massuda[6], Jamison Sloan[1], Nicolas Romeo[2], Yang Yu[7], John D. Joannopoulos[2,3], Ido Kaminer[8], Steven G. Johnson[2,4], Marin Soljačić[1,2]

Bombardment of materials by high-energy particles often leads to light emission in a process known as scintillation. Scintillation has widespread applications in medical imaging, x-ray nondestructive inspection, electron microscopy, and high-energy particle detectors. Most research focuses on finding materials with brighter, faster, and more controlled scintillation. We developed a unified theory of nanophotonic scintillators that accounts for the key aspects of scintillation: energy loss by high-energy particles, and light emission by non-equilibrium electrons in nanostructured optical systems. We then devised an approach based on integrating nanophotonic structures into scintillators to enhance their emission, obtaining nearly an order-of-magnitude enhancement in both electron-induced and x-ray–induced scintillation. Our framework should enable the development of a new class of brighter, faster, and higher-resolution scintillators with tailored and optimized performance.

Scintillation, the process by which high-energy particles (HEPs, also known as ionizing radiation) bombarding a material convert their kinetic energy into light, is among the most commonly occurring phenomena in the interaction of ionizing radiation with matter. It enables a number of technologies, including x-ray detectors used in medical imaging and nondestructive inspection, γ-ray detectors in positron emission tomography scanners, phosphor screens in night-vision systems, electron detectors in electron microscopes, and electromagnetic calorimeters in high-energy physics experiments (*1*, *2*). Scintillation appears under many different guises. For example, when the "high-energy" particle is a visible or ultraviolet (UV) photon, the scintillation is better known as photoluminescence. When the incident particles are energetic electrons, scintillation is also known as incoherent cathodoluminescence. When the high-energy particle is an x-ray or γ-ray, the phenomenon is almost exclusively referred to as scintillation (*1*). Because of scintillation's broad applications, there is interest in the development of "better scintillators" with greater photon yields as well as greater spatial and energy resolution. Such enhanced scintillators could translate into enhanced functionalities. One such example is in medicine: Brighter and higher-resolution scintillators could enable medical imaging (e.g., computed tomography) with higher resolution and a substantially lower radiation dose. Current approaches to improve scintillation are mostly oriented toward the growth of higher-quality materials (e.g., single-crystalline, controlled creation of defect sites) as well as the identification of new materials [e.g., ceramics and metal halide perovskites (*3*)] with faster and brighter intrinsic scintillation.

We have developed a different approach to this problem, which we refer to as "nanophotonic scintillators." By patterning a scintillator on the scale of the wavelength of light, it is possible to strongly enhance, as well as control, the scintillation yield, spectrum, directivity, and polarization response. The motivation for our approach was the observation that the light emitted in scintillation is effectively spontaneous emission (*4*). An enormous amount of effort in multiple fields has gone into controlling and enhancing spontaneous emission through the density of optical states (*5*, *6*), with corresponding impact in those fields (*7*), including photovoltaics (*8*), sensing (*9*, *10*), light-emitting diodes (LEDs) (*11*, *12*), thermal emission (*13*), and free-electron radiation sources (*14*–*23*). In the context of scintillation, nanophotonic enhancements could in principle take two forms: (i) through direct enhancement of the rate of spontaneous emission by shaping the density of optical states (*4*), or (ii) through improved light extraction from bulk scintillators. Early work demonstrated enhanced light extraction provided by a photonic crystal coating atop a bulk scintillator (*24*–*30*). Nonetheless, the prospect of enhancing scintillation through the local density of states, as well as the prospect of large scintillation enhancements, by either mechanism remains unrealized. Moreover, the type of nanophotonic structures that could even in principle realize such effects is unknown.

Part of the reason for the lack of progress in this field so far entails a theoretical gap associated with the complex, multiphysics nature of scintillation emission (Fig. 1, A to D). The process of scintillation is composed of several complex parts spanning a wide range of length and energy scales (*1*): (i) ionization of electrons by HEP followed by production and diffusion of secondary electrons (Fig. 1B) (*31*, *32*); (ii) establishment of a non-equilibrium steady state (Fig. 1C) (*33*, *34*); and (iii) recombination, leading to light emission (Fig. 1D). The final step of light emission is particularly complex to model, especially in nanophotonic settings, as it results from fluctuating, spatially distributed dipoles with a non-equilibrium distribution function that strongly depends on the previous steps of the scintillation process.

A general theory of nanophotonic scintillation

First, we present a unified theory of nanophotonic scintillators. The theory we have developed is ab initio: It can, from first principles, predict the angle- and frequency-dependent scintillation from arbitrary scintillators (established and nascent), taking into account the three steps illustrated in Fig. 1, B to D. It takes into account the energy loss dynamics of HEPs through arbitrary materials, the non-equilibrium steady state and electronic structure of the scintillating electrons, and the nanostructured optical environment (i.e., the electrodynamics of the light emission by this non-equilibrium electron distribution).

Consider the situation depicted in Fig. 1A, in which a HEP beam deposits energy into a scintillating material (Fig. 1B). The material may be in proximity to a nanophotonic structure or integrated with it (as in both cases for which we present experiments). The interaction of the beam with the scintillating material will generally lead to a process of electron excitation in the scintillator, followed by relaxation into an excited state (Fig. 1C).

After this relaxation occurs, the occupations of electrons and holes are typically in an approximate equilibrium (*34*) (referred to as a non-equilibrium steady state). This equilibrium is well defined because it occurs on picosecond time scales, which are effectively instantaneous relative to the excited-state depletion time scales (nanoseconds) (*31*). Under these assumptions, the radiative recombination may be described in terms of emission from fluctuating currents in the material, not unlike thermal radiation (in which the electrons are in a true equilibrium). The key difference from thermal radiation is that the

[1]Research Laboratory of Electronics, Massachusetts Institute of Technology, Cambridge, MA 02139, USA. [2]Department of Physics, Massachusetts Institute of Technology, Cambridge, MA 02139, USA. [3]Institute for Soldier Nanotechnologies, Massachusetts Institute of Technology, Cambridge, MA 02139, USA. [4]Department of Physics, University of Hong Kong, Hong Kong, China. [5]Department of Mathematics, Massachusetts Institute of Technology, Cambridge, MA 02139, USA. [6]Microsystems Technology Laboratories, Massachusetts Institute of Technology, Cambridge, MA 02139, USA. [7]Raith America Inc., Troy, NY 12180, USA. [8]Department of Electrical and Computer Engineering, Technion, Haifa 32000, Israel.
***Corresponding author. Email: chrc@mit.edu (C.R.-C.); nrivera@mit.edu (N.R.)**
†These authors contributed equally to this work.

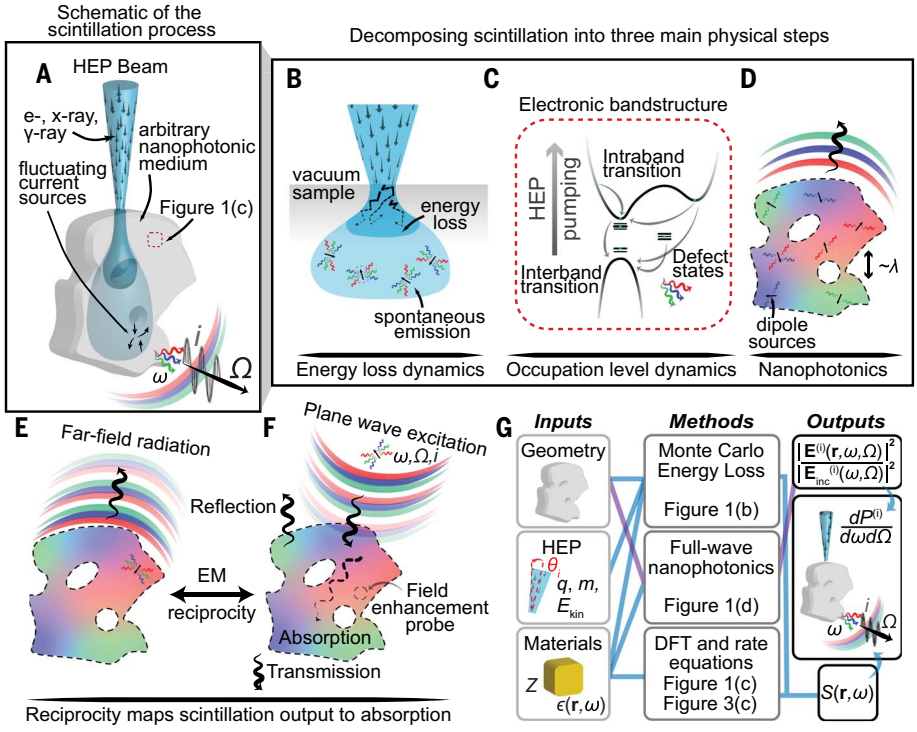

Fig. 1. A general framework for scintillation in nanophotonics. (**A**) We consider the case of high-energy particles (HEPs) bombarding an arbitrary nanophotonic medium, emitting scintillation photons at frequency ω (free-space wavelength λ), propagation angle Ω, and polarization *i*. (**B**) Subsequent HEP energy loss results in excitation of radiative sites (darker blue region in sample), which may diffuse before spontaneously emitting photons (lighter-blue region in sample). (**C**) The framework also accounts for different types of microscopic emitters. (**D**) The emitters may emit in arbitrary nanophotonic environments. (**E** and **F**) Electromagnetic reciprocity maps far-field radiation calculations from the stochastic many-body ensemble in a single electromagnetic simulation of plane-wave scattering (E) by calculating the effective spatially dependent field enhancement (F). (**G**) Summarized framework. Links indicate forward flow of information. The purple links indicate the possibility of backward flow (inverse design) in our current implementation. *q*, particle charge; *m*, mass; E_{kin}, kinetic energy; θ_i, incidence angle; $\varepsilon(\mathbf{r},\omega)$, material permittivity; *Z*, effective *Z*-number; $S(\mathbf{r},\omega)$, spatially varying intrinsic scintillation spectral function; $dP^{(i)}/d\omega d\Omega$, scintillation spectral-angular power density at polarization *i*. See (*39*) for an expanded and elaborated version of this panel.

occupation functions that determine the current-current correlations (which in turn determine the emission) are no longer governed by the Bose-Einstein distribution, but are instead dependent on the material and the HEP pump (and therefore spatially dependent).

Despite the nonuniversality of the current-current correlations, the otherwise strong similarity to thermal radiation inspires a key simplification that also gives rise to simple and powerful numerical methods for modeling and optimizing scintillation. This key simplification is electromagnetic reciprocity, which relates the following two quantities: (i) the emitted scintillation from the structure (at a given frequency ω, direction Ω, and polarization *i*) and (ii) the intensity of the field induced in the scintillator by sending a plane wave at it (of frequency ω, propagating along direction Ω into the structure, and polarization *i*). The intensity of the field induced in the structure at a given point is proportional to the local absorption, so the "emission" (i) is related to "absorption" of a plane wave (ii). As a result of this relation, it is possible to calculate the scintillation at some angle and frequency by calculating absorption of light incident from the far field at that frequency, angle, and polarization. We note that this relation makes use of the Lorentz reciprocity of Maxwell's equations only for the nanophotonic structure, and thus makes no assumption about the electronic transitions responsible for scintillation (we assume that the non-equilibrium electrons only weakly change the material's optical properties). Lorentz reciprocity can be broken in several classes of systems such as magnetic, nonlinear, and time-modulated materials (*35*). Such nonreciprocal photonic structures, which are of great recent interest, require extension of the framework but may allow many new phenomena [as in nonreciprocal effects in thermal radiation (*36*)]. Direct modeling of light emission by means of calculating the emission from an ensemble of fluctuating dipoles, as considered in the past [e.g., for thermal emission (*37*)], is extremely resource-intensive from a computational perspective (*38*). The effect of the spatial distribution of the scintillating centers is captured by integrating this spatial distribution against the spatially dependent absorption in the scintillating structure. In this way, the spatial information can be obtained "all-at-once" from a single absorption "map."

We use this simplification to quantify scintillation, which we represent in terms of the scintillation power per unit frequency $d\omega$ and solid angle $d\Omega$ along the *i*th polarization (e.g., $i = s,p$): $dP^{(i)}/d\omega d\Omega$ [where $dP/d\omega d\Omega = \sum_i (dP^{(i)}/d\omega d\Omega)$ is the total scintillation power density]. In most cases, the current-current correlations in the scintillator are isotropic [a condition that we relax in (*39*)], and we get

$$\frac{dP^{(i)}}{d\omega d\Omega} = \frac{\omega^2}{8\pi^2\varepsilon_0 c^3}\int d\mathbf{r}\,\frac{\left|\mathbf{E}^{(i)}(\mathbf{r},\omega,\Omega)\right|^2}{\left|\mathbf{E}^{(i)}_{\mathrm{inc}}(\omega,\Omega)\right|^2}\,S(\mathbf{r},\omega) \tag{1}$$

where the quantity $\mathbf{E}^{(i)}_{\mathrm{inc}}(\omega,\Omega)$ denotes the electric field of an incident plane wave of frequency ω, incident from a direction Ω, with polarization *i*. The quantity $\mathbf{E}^{(i)}(\mathbf{r},\omega,\Omega)$ denotes the total electric field at position $\mathbf{r}$ resulting from the incident field, and their ratio is thus the field enhancement. The function $S(\mathbf{r},\omega)$ in Eq. 1 is the spectral function encoding the frequency and position dependence of the current-current correlations, given by

$$S(\mathbf{r},\omega) = \frac{1}{3}\sum_{\alpha,\beta}\mathrm{tr}\left[\mathbf{J}^{\alpha\beta}(\mathbf{r})\mathbf{J}^{\beta\alpha}(\mathbf{r})\right]\times f_\alpha(\mathbf{r})\left[1-f_\beta(\mathbf{r})\right]\delta(\omega-\omega_{\alpha\beta}) \tag{2}$$

In this spectral function, f_α is the occupation factor of microscopic state α with energy E_α, $\mathbf{J}^{\alpha\beta}$ represents the matrix element of the current density operator [$\mathbf{J} \equiv (e/m)\psi^\dagger(-i\hbar\nabla)\psi$], $\omega_{\alpha\beta} = [E_\alpha - E_\beta]/\hbar$, and tr denotes matrix trace. Besides the position dependence of the current density matrix element, the occupation functions can also depend on position, as they depend on the HEP energy loss density (specifically, how much energy is deposited in the vicinity of $\mathbf{r}$). Interestingly, Eq. 1 would be proportional to the strength of thermal emission upon substitution of $S(\mathbf{r},\omega)$ by the imaginary part of the material permittivity, multiplied by the Planck function. However, here the primary difference is that $S(\mathbf{r},\omega)$ describes a non-equilibrium state rather than the thermal equilibrium state of the material.

To better understand the core components of nanophotonic scintillation enhancement, let us simplify it further by considering the case where the density of excited states is uniform over some scintillating volume V_S [in which case we may drop the spatial dependence of *S* such that $S(\mathbf{r},\omega) \rightarrow S(\omega)$]. This volume can be thought of as the characteristic volume

over which excited electrons are created (as in Fig. 1B). Then we may write

$$\frac{dP^{(i)}}{d\omega d\Omega} = \frac{\pi}{\varepsilon_0 \omega} \times S(\omega) \times \frac{V_{\text{eff}}^{(i)}(\omega, \Omega)}{\lambda^3} \quad (3)$$

where

$$V_{\text{eff}}^{(i)}(\omega, \Omega) = \int_{V_S} d\mathbf{r} \frac{\left|\mathbf{E}^{(i)}(\mathbf{r}, \omega, \Omega)\right|^2}{\left|\mathbf{E}_{\text{inc}}^{(i)}(\omega, \Omega)\right|^2} \quad (4)$$

Because $V_{\text{eff}}^{(i)}(\omega, \Omega)$ has dimensions of volume and is proportional to the absorbed power over V_S (in the limit of weak absorption, so as not to perturb the field solutions), we often refer to this term (shortened as V_{eff}) as the effective volume of field enhancement or the effective volume of absorption. Equation 3 states that under this approximation, the scintillation spectrum is a simple product of a microscopic factor [which is set by the non-equilibrium spectral function $S(\omega)$] and an effective absorption volume V_{eff} [which is set only by the (structured) optical medium surrounding the scintillating medium].

Our framework to calculate scintillation according to Eq. 1 consists of three components, as illustrated in Fig. 1, B, C, D, and G: energy loss of a beam of HEPs, creation of excited electrons, and subsequent light emission (which is computed by calculating field enhancement from incident plane waves via electromagnetic reciprocity). As a technical matter, we note that we compute the HEP energy loss density by Monte Carlo simulations of energy loss [as is standard; see (*40*)], the electron energy levels and spectral function through density functional theory (DFT), and the nanophotonic field enhancement through finite-difference time-domain and rigorous coupled-wave analysis methods. In principle, these components are coupled together (*39*).

More details on each component of the workflow depicted in Fig. 1G can be found in (*39*). The description of scintillation provided here—using calculations of electronic structure, energy loss, and electromagnetic response—is, to the best of our knowledge, the first to provide an ab initio and end-to-end account of scintillation in nanophotonic structures.

Enhancement and shaping of electron beam–induced scintillation

We first experimentally demonstrate scintillation from silicon-on-insulator nanophotonic structures due to bombardment by electrons (here, with energies in the range of 10 to 40 keV). Electrons with a few tens of keV energies are a convenient platform to demonstrate nanophotonic scintillation, as they readily lose almost all of the energy to the nanophotonic structure. Such lower-energy particles penetrate materials less deeply, leading to a strong overlap between the spatial region of HEP energy loss density and the region of high field enhancement (the latter of which is within a few hundred nanometers of the surface).

Our experimental setup to measure scintillation is based on a modified scanning electron microscope (SEM) [an earlier version of which was reported in (*15*–*17*, *19*)], shown in Fig. 2, A and E: A focused electron beam of tunable energy (10 to 40 keV) excites the sample at a shallow (~1°) angle, and the resulting radiation is collected and analyzed with a set of free-space optics. The light is collected by an objective lens that accepts radiation emitted in a cone of half-angle 17.5°. Under the shallow-angle conditions of electron incidence in our experiments, the effective penetration depth of the electrons is on the scale of a few hundred nanometers (Fig. 2B), far below the nominal mean free paths of 40-keV electrons in silica or silicon, which are on the order of 20 μm. This leads to strong overlap of the energy loss with regions of field enhancement. Control over the incidence angle also enables tuning of this overlap between the HEP energy loss density and V_{eff}.

The first structure we consider is a thin film of 500 nm of Si atop 1 μm of SiO_2 atop a Si substrate. The second structure differs from the first in that the top Si layer is patterned to form a square lattice (design period ~430 nm; see Fig. 2C) of air holes (diameter ~260 nm) of various etch depths (~25, 35, and 45 nm). We refer to them as "thin film" (TF) and "photonic crystal" (PhC) samples, respectively. Scintillation in these structures occurs in the buried silica layer, and in particular among a class of commonly occurring defects called self-trapped holes (STHs) (*41*). Such defects have been studied extensively because of their consequences for silica fibers. They display distinct emission at red and green wavelengths, which, in addition to our other observations, enable us to attribute our observations to STH scintillation [and thus rule out other mechanisms of electron beam–induced emission, such as coherent cathodoluminescence (*39*)].

We now show how nanophotonic structures shape and enhance scintillation in silica. The scintillation spectrum of the sample in the visible range, for both TF and PhC samples, is shown in Fig. 2D. The TF scintillation measurements shown in black in Fig. 2, F and G, display two main sets of features at green (~500 nm) and red (~625 to 675 nm) wavelengths. At red wavelengths, there is a clear double-peak structure; at green wavelengths, the scintillation spectrum displays multiple peaks. These multiply peaked spectra differ considerably from prior observations of STH scintillation (*41*): Although they occur at roughly the same wavelength, prior observations show only one peak at the red and green wavelengths (*42*). The multiple peaks of the spectrum (and even its shoulders) are well accounted for at both red and green wavelengths even by the simplified Eq. 3, and specifically by multiplying the shape of the STH spectrum in bulk by the V_{eff} calculated for the TF. The bulk spectrum is inferred from previous observations (*41*) and is confirmed by our DFT calculations (Fig. 3D). The multiply peaked structure of V_{eff} thus arises from thin-film resonances, which enhance the absorption of light in the buried silica layer. The agreement between theory and experiment in Fig. 2, F and G, unambiguously indicates a strong degree of spectral control over scintillation even in the simplest possible "nanostructure" (namely, a thin film).

In contrast to the TF scintillation, the scintillation from the PhC samples displays very strong and spectrally selective enhancement. We report an enhancement of the red scintillation peak in the PhC sample, relative to the TF, by a factor of ~6 (peak at 674 nm) and a factor of ~3 integrated over the main red peak (665 ± 30 nm), as shown in Fig. 2D. This feature is reproduced by our theoretical framework via enhancement of V_{eff} around the red scintillation peak, using the same fitting parameters as those taken from the TF results of Fig. 2, F and G. Comparatively, the green peak remains at a value similar to those in the TF spectra. As a result of the high losses at those shorter wavelengths, little enhancement is expected for the green wavelength.

The observed enhancement can readily be attributed theoretically to the presence of high–quality factor (high-Q) resonances at the red wavelength, which lead to enhanced absorption of light in the far field. The positions of the many subpeaks in the scintillation spectra are accounted for by the peaks of V_{eff}. Somewhat larger uncertainties are introduced in the patterned structure because of the strong degree of angular shaping of the radiation associated with certain wave vectors in the PhC band structure (Fig. 2G, inset, shows the predicted scintillation spectrum at normal emission). As a result, the spectrum depends on the exact angular acceptance function of the objective. There is also a more sensitive dependence on the exact distribution of electron energy loss relative to the thin-film case; this is due to the well-localized nature of the resonances leading to scintillation in the patterned structure.

Having shown scintillation control and enhancement based on nanophotonic structures, we now explore another core element of our general framework for scintillation: the microscopic transition dynamics associated with the scintillation process, their effect on the non-equilibrium occupation functions, and the corresponding effect on observable properties of the scintillation spectrum. In the specific case of silica defects, we can make use of spectral observables such as dependence of the

scintillation on the electron energy, as well as the ratio of green to red scintillation peak powers (defined as η) as a function of deposited HEP energy, to test assumptions about the microscopic properties of the scintillation mechanism. We can even infer the energy level structure of the scintillating defects by combining these measurements with first-principles electronic structure calculations and models of the excited electron kinetics (e.g., rate equations).

Figure 3A shows the evolution of the scintillation spectrum for various energies. At high-energy pumping (~40 keV), red scintillation in the PhC sample dominates; decreasing the pumping energy results in a gradual increase of the green peak scintillation (and of η). We took similar measurements for high- and low-current pumping (at a constant pumping energy of 40 keV) of PhC and TF samples. Our results are compiled in Fig. 3E, where the green peak scintillation always dominates ($\eta > 1$) for the TF sample, whereas a crossover is seen for a certain value of the deposited beam power (represented by η crossing unity) for the PhC sample.

To account for these observations, we consider a description of the defect levels in terms of a three-level Fermi system, featuring two lowest occupied levels (denoted 1 and 2 in Fig. 3C) coupled to an upper "pump" level (denoted 3) through the high-energy electron beam, which acts as a pump. These three levels correspond to energy levels from our electronic structure calculations of the STH defects in silica [based on DFT (*39*)]. The relative rates of the transitions $3 \rightarrow 1$ (Γ_{31}) and $3 \rightarrow 2$ (Γ_{32})—which depend on the pump strength and the emission rates (which in turn depend on V_{eff})—dictate the strength of the green and red emission, respectively. We arrive at the results of Fig. 3E by solving for the steady-state values of these transition rates using rate equations (*39*) and extracting the corresponding η as a function of the incident beam power.

The agreement between theory and experiment enables us to understand the crossover as resulting from a combination of (i) the relative enhancement of red transitions from the PhC, and (ii) the nonlinear transition dynamics of excited electrons in the defect. In particular, data from both samples indicate that the pump rate for the "green transition," Γ_{13}, is faster than its red counterpart, Γ_{23} (with consistent ratio values of ~3.2 for the TF and ~3.35 for the PhC). The existence of a crossover-deposited beam power between domains where $\eta > 1$ and $\eta < 1$ translates into an enhancement of the ratio of decay rates Γ_{32}/Γ_{31} in the PhC sample. After comparing model parameters

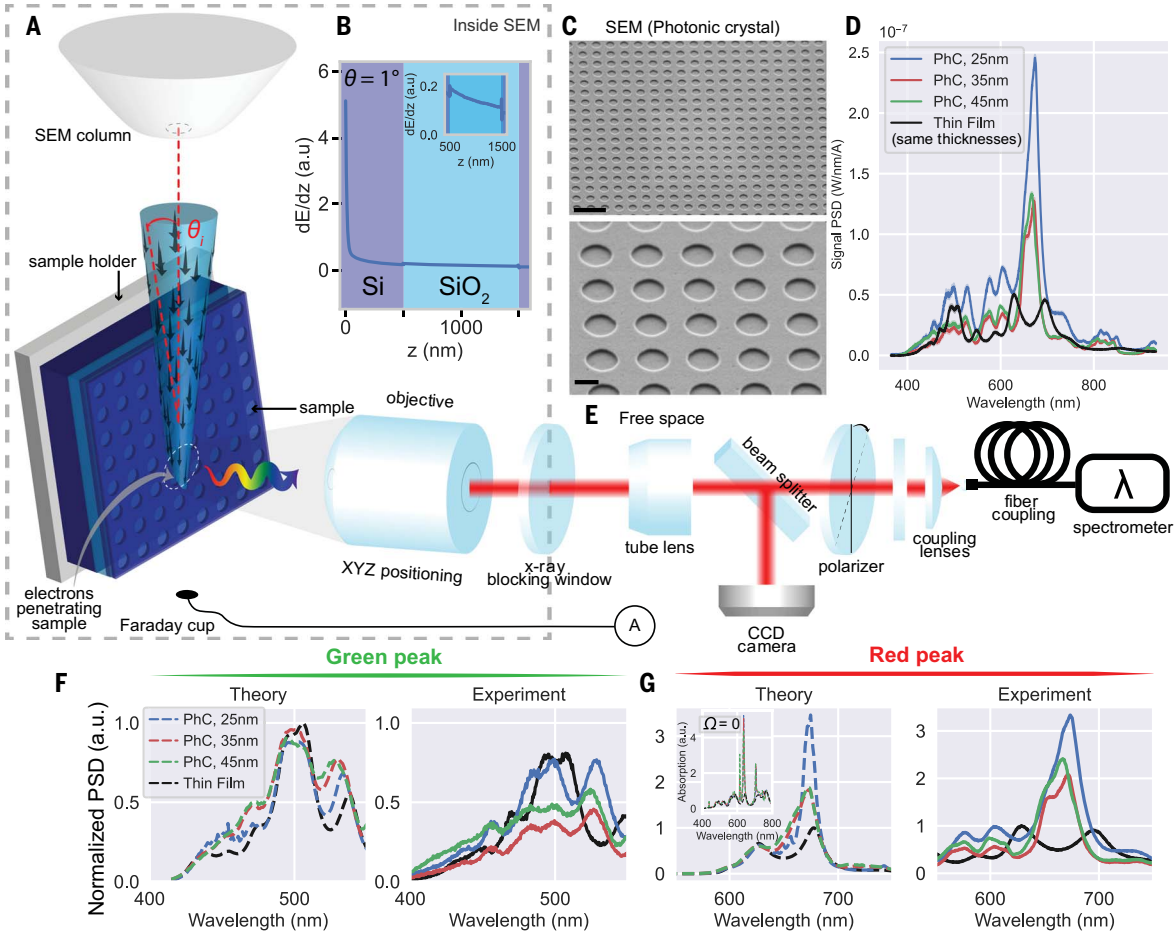

Fig. 2. Experimental demonstration of nanophotonic shaping and enhancement of electron beam–induced scintillation. (**A**) A modified scanning electron microscope (SEM) is used to induce and measure scintillation from electron beams (10 to 40 keV) bombarding scintillating nanophotonic structures. (**B**) Electron energy loss in the silicon-on-insulator wafer is calculated via Monte Carlo simulations. Inset: Zoomed-in electron energy loss in the scintillating (silica) layer. a.u., arbitrary units. (**C**) SEM images of photonic crystal (PhC) sample (etch depth 35 nm). Tilt angle 45°. Scale bars, 1 μm (top), 200 nm (bottom). (**D**) Scintillation spectrum from thin-film and PhC samples with varying etch depths (but same thickness). PSD, power spectral density. (**E**) The scintillation signal is coupled out of the vacuum chamber with an objective and then imaged on a camera and analyzed with a spectrometer. (**F** and **G**) Comparison between theoretical (left) and experimental (right) scintillation spectra for green and red scintillation peaks. Inset: Calculated scintillation spectra (per solid angle) at normal emission direction, showing the possibility of much larger enhancements over a single angle of emission.

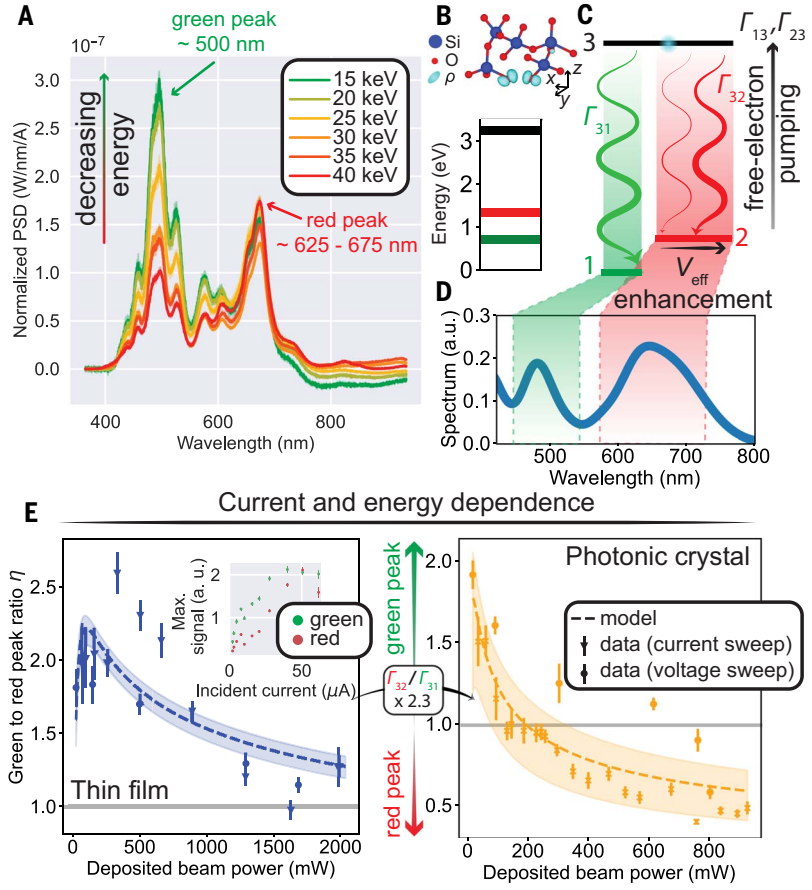

Fig. 3. Probing the microscopics of electron beam–induced scintillation in silica. (**A**) Energy-dependent scintillation spectra (PhC sample, etch 25 nm). (**B**) Top: 3D molecular model of STH defect in silica; ρ, spin-polarized density. Bottom: Calculated STH defect energy levels via density functional theory (DFT). (**C**) Simplified three-level system modeling the microscopics of scintillation from STH defects in silica. (**D**) Bulk scintillation spectrum calculated with DFT (dipole matrix elements). (**E**) Thin film (left) and PhC (right) scintillation peak ratios as a function of deposited beam powers through electron pumping. The dashed line corresponds to the mean model prediction and the shaded area to the prediction from the model parameters ± SD [defined as the uncertainty on Γ_{31}/Γ_{32}, the ratio of rates shown in (B), bottom]. Inset: Maximum signal of green and red scintillation peaks versus current in TF sample.

fitting the TF experimental data to models fitting the PhC data, we estimate that the decay rate ratio is enhanced by a factor of ~2.3 ± 1.0. This value is in agreement with the V_{eff} enhancement predicted by our theory and by our observation of enhanced scintillation from the red defects in the experimental data.

By patterning nanophotonic scintillators, one can thus tailor microscopic properties and selectively enhance scintillation from microscopic defects. This also suggests that scintillation rates can be selectively enhanced using nanophotonic structures, a feature that is particularly sought after in some medical imaging modalities (*43*). Moreover, our results indicate that the measured scintillation may be used to sort out competing models of the electronic structure, especially in complex defects such as this one, where self-interaction effects lead to modeling difficulties (*39*).

Observation of strongly enhanced scintillation induced by x-rays

We now consider another example of a nanophotonic scintillator designed using our theoretical framework, showing its application to enhancing scintillation induced by high-energy photons such as x-rays. Such HEPs lose their energy much differently from massive charged particles (such as electrons).

In our experimental configuration (Fig. 4A), x-rays traverse a specimen, leading to spatially dependent absorption of the incident x-ray flux. This absorption pattern is geometrically magnified until it encounters the cerium-doped yttrium-aluminum-garnet (YAG:Ce) scintillator. The pattern is then translated into scintillation photons, which are imaged with an objective and a charge-coupled device (CCD) camera. The nanopatterned scintillator is constructed by etching a two-dimensional PhC into YAG [via focused ion beam (FIB) lithography (*39*)] at the surface of the scintillator facing the objective. The PhC period is 430 nm and the total patterned area is 215 μm × 215 μm (Fig. 4) or 430 μm × 430 μm (Fig. 5).

In the case of YAG:Ce, the intrinsic scintillation properties have long been characterized and our experiments reveal only weak dependence of the scintillation on incident x-ray energy (*39*). Thus, the full theoretical apparatus we demonstrate for electron scintillation is not needed to adequately describe our results. Primarily, the electromagnetic response (using reciprocity) is needed to account for the experimental results and is the part of our general framework that leads us to order-of-magnitude enhancement of x-ray scintillation (*39*).

According to the scintillation framework developed above, nanophotonic scintillation enhancement is to be expected when the absorption of light is enhanced. In Fig. 4B, we show the calculated wavelength-dependent scintillation in YAG:Ce (averaged over the angular acceptance of the objective, as in Fig. 2) for an unpatterned self-standing thick (20 μm) film, as well as for the PhC sample. Here, the calculated enhancement is by a factor of ~9.3 ± 0.8 over the measured scintillation spectrum. In our calculations, we attribute the main error bar to the uncertainty on the hole depth [±10 nm, as can be extracted from our atomic force microscopy (AFM) measurements, shown fully in Fig. 4A (right) and in cross sections in (*39*)]. However, there are several other sources of uncertainty in the fabricated samples: the hole diameter, the hole periodicity, and the optical absorption of YAG:Ce (taken in our calculations to be the value provided by the wafer supplier). We also measured, and compared to our theory, scintillation enhancements from multiple nanophotonic scintillators with various thicknesses, hole shapes, depths, and patterned areas (table S1) (*39*).

Here, the x-ray scintillation enhancement originates in light out-coupling enhancement (or, by reciprocity, in-coupling enhancement). In particular, the PhC allows more channels (i.e., a plane-wave coupling to a resonance) into the scintillator crystal than would be achievable with a flat interface. The multiple channels translate into sharp resonant peaks in the calculated absorption spectrum [see (*39*) for raw signal]. This is to be contrasted with the origin of electron beam–induced scintillation enhancement in silica, where the enhancement can be tied to the presence of one or a small number of high-Q resonances. This effect is of the type often leveraged to design more efficient LEDs and solar cells that approach the "Yablonovitch limit" in both ray-optical (*44*, *45*) and nanophotonic (*46*, *47*) settings. There, it is well known that the device efficiency is optimized by designing a structure

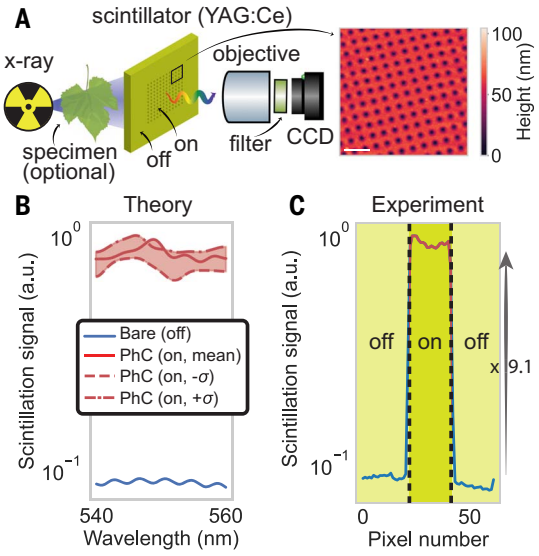

Fig. 4. Nanophotonic enhancement of x-ray scintillation. (**A**) Left: X-ray scintillation experimental setup. Light generated by x-ray bombardment of a YAG:Ce scintillator is imaged with a set of free-space optics. A specimen may be positioned between the source and the scintillator to record an x-ray scan of the specimen. Right: AFM image of patterned YAG:Ce scintillator (thickness, 20 μm). Scale bar, 1 μm. (**B**) Calculated scintillation spectrum of the PhC, integrated over the experimental angular aperture. Calculations are performed for measured etching depths ± SD (corresponding to 40, 50, and 60 nm). The shaded area corresponds to possible scintillation enhancements between those values. The calculated spectra are convolved with a moving-mean filter of width 1.33 nm [raw signal shown in (*39*)]. (**C**) Measured scintillation along a line of the sample, including regions on (red) and off (blue) the PhC. The scintillation from the PhC region is on average higher than the unpatterned region by a factor of ~9.1. All signals were recorded with x-ray source settings of 40 kVp, 3 W.

that leads to strong absorption over the spectral range of the emission (*44*, *48*).

In Fig. 4C, we show the experimentally measured scintillation scanned along a line of the sample. The regions "off" indicate unpatterned regions of the YAG:Ce, whereas "on" indicates the PhC region. Here, the signal is enhanced on average by a factor of ~9.1 over the unpatterned region, consistent with the predictions of Fig. 4B.

To demonstrate the potential of our approach to x-ray imaging, we fabricated a larger-scale pattern on a 50-μm wafer, which exhibits a scintillation enhancement of 2.3 (*39*). We recorded single-shot x-ray scans of biological and inorganic specimens through the PhC, showing no evident decrease in resolution, while increasing the image brightness by the same factor. Equivalently, the required x-ray dose or exposure time to get a given number of counts on the detector is reduced [shown experimentally in (*39*)].

Our framework allows us to further gain understanding of the scintillation mechanism at play, directly leveraging known techniques in absorption enhancement. For certain structures, one could expect even greater scintillation enhancements on the order of ~$4n^2$ in the ray-optics approximation (*44*) or ~$4\pi n^2$ for periodic structures on the wavelength scale (*46*, *47*) (where n is the index of refraction). For example, for a thin high-index material such as doped GaAs, which also scintillates at room temperature (*49*), enhancements on the order of ~50 and ~150 could be respectively achieved in the two regimes (over a 2π collection solid angle).

Discussion

We have presented a general framework to model, tailor, and enhance scintillation by means of nanophotonic structures integrated into scintillating materials (nanophotonic scintillators). Although we mainly focused on the demonstration of spectral shaping and enhancement of scintillation, our results could be extended to show angular and polarization control as well. We have demonstrated nanophotonic scintillators enhancing electron beam–induced and x-ray–induced scintillation. The theoretical framework we used to describe our experimental results combines Monte Carlo simulations of the energy loss density (*40*) with DFT calculations of the microscopic structure and full-wave calculations of the electromagnetic response of the nanophotonic structures probed in this work.

We note that this type of "full" analysis, to the best of our knowledge, has not been performed to explain scintillation (nor incoherent cathodoluminescence) experiments, likely because of the prohibitively expensive computations associated with simulating ensembles of dipoles radiating in 3D structures. The reciprocity framework we use [also commonly used in areas of thermal radiation, LEDs, and photoluminescence (*34*, *50*–*54*)] strongly simplifies the analysis, and makes a full modeling of the scintillation problem tractable. We conclude by outlining a few promising avenues of future work that are enabled by the results provided here. [See (*39*) for further elaboration and initial results for each of these avenues.]

The first area, inspired by our simplified calculations based on reciprocity, is numerical optimization of nanophotonic scintillators. Our framework, which relies on the calculation of V_{eff} (which is relatively amenable, even in three dimensions), enables the inverse design of nanophotonic scintillators. [See (*39*) for methods to calculate the forward (V_{eff} given a nanophotonic structure) and backward (gradients of V_{eff} with respect to degrees of freedom describing the nanophotonic structure) problems.] The experimentally reported enhancements can be further improved upon by inverse-designing the nanophotonic structure via topology optimization of V_{eff} (*55*). In (*39*), we show the kind of results that could be expected from topology-optimized nanophotonic scintillators: We find that selective enhancements of scintillation in particular topology-optimized photonic structures by one to nearly two orders of magnitude are possible. By considering different emission linewidths and frequencies, one can selectively design optimized nanophotonic structures that enhance one of the scintillating peaks, at a single frequency or over the entire scintillation bandwidth. Beyond our reciprocity-based approach, low-rank methods can be used for the inverse design of nanophotonic scintillators with very large angular ranges (*56*, *57*). Beyond scintillation, our techniques may find applicability in other imaging modalities involving random incoherent emitters, such as surface-enhanced Raman scattering (*58*).

Another promising area of research enabled by our findings is nanophotonically enhanced and controlled UV light sources. In (*39*) we show how UV scintillation in patterned materials such as hBN enables strongly enhanced scintillation with a spectrum that can be controlled simply by the position of the electron beam relative to the patterned features in the hBN arising from changes in the overlap between the HEP loss density and V_{eff}. The prospect of realizing optimized and compact nanophotonic UV scintillation sources is particularly exciting for applications in water purification and sanitization (*59*).

Nanophotonic scintillators provide a versatile approach for controlling and enhancing the performance of scintillating materials for a wide range of applications. The framework developed here applies to arbitrary scintillating

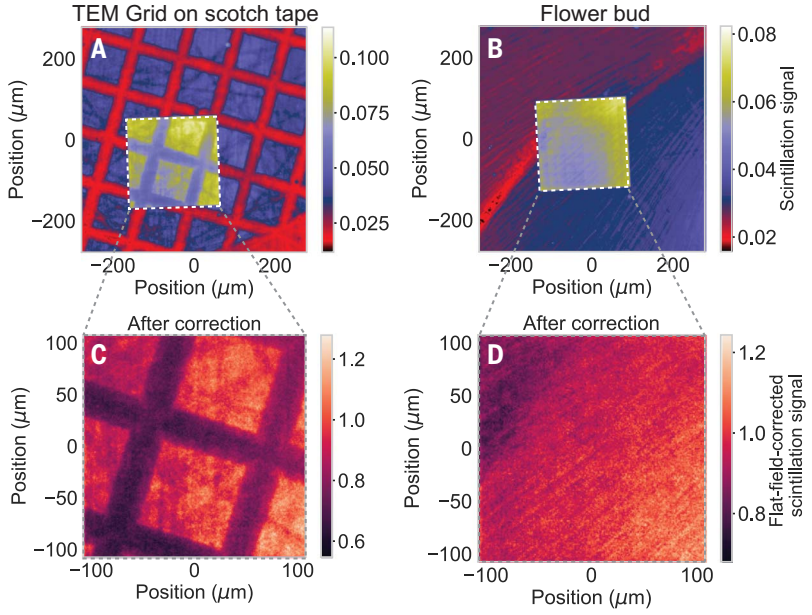

Fig. 5. X-ray scintillation imaging with nanophotonic scintillators. (**A** and **B**) Measured x-ray images of a TEM grid on scotch tape (A) and a flower bud (B). The white square delimits the PhC area. (**C** and **D**) Flat field–corrected zoom-in of the x-ray image in the PhC area. Geometric magnification on those images is ~2. Relative to the unpatterned regions, the images are brighter above the PhC region, showing no evident decrease in resolution. The particular nanophotonic scintillator used for this experiment was patterned over an area of 430 μm × 430 μm and resulted in a scintillation enhancement of ×2.3 (measured with respect to an unpatterned scintillator of same thickness). All signals were recorded with x-ray source settings of 60 kVp, 5 W.

materials, nanophotonic structures, and HEPs, solving for the process end-to-end using first-principles methods. The electron-beam and x-ray scintillation experiments provide the proof-of-concept tests of the promising prospects of this field. Our work may open a panoply of exciting applications, from high-resolution, low-dose x-ray imaging to efficient UV electron beam–pumped light sources.

REFERENCES AND NOTES

1. A. Gektin, M. Korzhik, *Inorganic Scintillators for Detector Systems* (Springer, 2017).
2. S. Cherry, J. Sorenson, M. Phelps, *Physics in Nuclear Medicine* (Wiley, 2012).
3. Q. Chen *et al*., All-inorganic perovskite nanocrystal scintillators. *Nature* **561**, 88–93 (2018). doi: 10.1038/s41586-018-0451-1; pmid: 30150772
4. Y. Kurman, A. Shultzman, O. Segal, A. Pick, I. Kaminer, Photonic-Crystal Scintillators: Molding the Flow of Light to Enhance X-Ray and γ-Ray Detection. *Phys. Rev. Lett.* **125**, 040801 (2020). doi: 10.1103/PhysRevLett.125.040801; pmid: 32794818
5. E. Yablonovitch, Inhibited spontaneous emission in solid-state physics and electronics. *Phys. Rev. Lett.* **58**, 2059–2062 (1987). doi: 10.1103/PhysRevLett.58.2059; pmid: 10034639
6. J. D. Joannopoulos, S. G. Johnson, J. N. Winn, R. D. Meade, *Photonic Crystals: Molding the Flow of Light* (Princeton Univ. Press, 2011).
7. M. Pelton, Modified spontaneous emission in nanophotonic structures. *Nat. Photonics* **9**, 427–435 (2015). doi: 10.1038/nphoton.2015.103
8. A. Polman, H. A. Atwater, Photonic design principles for ultrahigh-efficiency photovoltaics. *Nat. Mater.* **11**, 174–177 (2012). doi: 10.1038/nmat3263; pmid: 22349847
9. P. Anger, P. Bharadwaj, L. Novotny, Enhancement and quenching of single-molecule fluorescence. *Phys. Rev. Lett.* **96**, 113002 (2006). doi: 10.1103/PhysRevLett.96.113002; pmid: 16605818
10. J. B. Jackson, N. J. Halas, Surface-enhanced Raman scattering on tunable plasmonic nanoparticle substrates. *Proc. Natl. Acad. Sci. U.S.A.* **101**, 17930–17935 (2004). doi: 10.1073/pnas.0408319102; pmid: 15608058
11. E. F. Schubert *et al*., Highly efficient light-emitting diodes with microcavities. *Science* **265**, 943–945 (1994). doi: 10.1126/science.265.5174.943; pmid: 17782147
12. A. A. Erchak *et al*., Enhanced coupling to vertical radiation using a two-dimensional photonic crystal in a semiconductor light-emitting diode. *Appl. Phys. Lett.* **78**, 563–565 (2001). doi: 10.1063/1.1342048
13. J.-J. Greffet *et al*., Coherent emission of light by thermal sources. *Nature* **416**, 61–64 (2002). doi: 10.1038/416061a; pmid: 11882890
14. R. Remez *et al*., Spectral and spatial shaping of Smith-Purcell radiation. *Phys. Rev. A* **96**, 061801 (2017). doi: 10.1103/PhysRevA.96.061801
15. Y. Yang *et al*., Maximal spontaneous photon emission and energy loss from free electrons. *Nat. Phys.* **14**, 894–899 (2018). doi: 10.1038/s41567-018-0180-2
16. I. Kaminer *et al*., Spectrally and Spatially Resolved Smith-Purcell Radiation in Plasmonic Crystals with Short-Range Disorder. *Phys. Rev. X* **7**, 011003 (2017). doi: 10.1103/PhysRevX.7.011003
17. C. Roques-Carmes *et al*., Towards integrated tunable all-silicon free-electron light sources. *Nat. Commun.* **10**, 3176 (2019). doi: 10.1038/s41467-019-11070-7; pmid: 31320664
18. F. Liu *et al*., Integrated Cherenkov radiation emitter eliminating the electron velocity threshold. *Nat. Photonics* **11**, 289–292 (2017). doi: 10.1038/nphoton.2017.45
19. A. Massuda *et al*., Smith-Purcell radiation from low-energy electrons. *ACS Photonics* **5**, 3513–3518 (2018). doi: 10.1021/acsphotonics.8b00743
20. F. J. García de Abajo, Optical excitations in electron microscopy. *Rev. Mod. Phys.* **82**, 209–275 (2010). doi: 10.1103/RevModPhys.82.209
21. G. Li, B. P. Clarke, J.-K. So, K. F. MacDonald, N. I. Zheludev, Holographic free-electron light source. *Nat. Commun.* **7**, 13705 (2016). doi: 10.1038/ncomms13705; pmid: 27910853
22. C. I. Osorio, T. Coenen, B. J. M. Brenny, A. Polman, A. F. Koenderink, Angle-Resolved Cathodoluminescence Imaging Polarimetry. *ACS Photonics* **3**, 147–154 (2015). doi: 10.1021/acsphotonics.5b00596
23. Y. Yang *et al*., Observation of enhanced free-electron radiation from photonic flatband resonances. arXiv 2110.03550 (2021).
24. X. Chen *et al*., Enhanced light extraction of plastic scintillator using large-area photonic crystal structures fabricated by hot embossing. *Opt. Express* **26**, 11438–11446 (2018). doi: 10.1364/OE.26.011438; pmid: 29716062
25. A. Knapitsch *et al*., Results of Photonic Crystal Enhanced Light Extraction on Heavy Inorganic Scintillators. *IEEE Trans. Nucl. Sci.* **59**, 2334–2339 (2012). doi: 10.1109/TNS.2012.2184556
26. A. Knapitsch, P. Lecoq, Review on photonic crystal coatings for scintillators. *Int. J. Mod. Phys. A* **29**, 1430070 (2015). doi: 10.1142/S0217751X14300701
27. Z. Zhu *et al*., Enhanced light extraction of scintillator using large-area photonic crystal structures fabricated by soft-X-ray interference lithography. *Appl. Phys. Lett.* **106**, 241901 (2015). doi: 10.1063/1.4922699
28. P. Pignalosa, B. Liu, H. Chen, H. Smith, Y. Yi, Giant light extraction enhancement of medical imaging scintillation materials using biologically inspired integrated nanostructures. *Opt. Lett.* **37**, 2808 (2012). doi: 10.1364/OL.37.002808; pmid: 22825141
29. Z. Zhu *et al*., Improved light output from thick β-Ga_2O_3 scintillation crystals via graded-refractive-index photonic crystals. *Opt. Express* **29**, 18646 (2021). doi: 10.1364/OE.428671; pmid: 34154117
30. X. Ouyang *et al*., Enhanced light output of CsI(Na) scintillators by photonic crystals. *Nucl. Instrum. Methods Phys. Res. A* **969**, 164007 (2020). doi: 10.1016/j.nima.2020.164007
31. C. A. Klein, Bandgap Dependence and Related Features of Radiation Ionization Energies in Semiconductors. *J. Appl. Phys.* **39**, 2029 (1968). doi: 10.1063/1.1656484
32. A. Polman, M. Kociak, F. J. García de Abajo, Electron-beam spectroscopy for nanophotonics. *Nat. Mater.* **18**, 1158–1171 (2019). doi: 10.1038/s41563-019-0409-1; pmid: 31308514
33. P. Wurfel, The chemical potential of radiation. *J. Phys. C* **15**, 3967–3985 (1982). doi: 10.1088/0022-3719/15/18/012
34. J. J. Greffet, P. Bouchon, G. Brucoli, F. Marquier, Light Emission by Nonequilibrium Bodies: Local Kirchhoff Law. *Phys. Rev. X* **8**, 021008 (2018). doi: 10.1103/PhysRevX.8.021008
35. D. L. Sounas, A. Alù, Non-reciprocal photonics based on time modulation. *Nat. Photonics* **11**, 774–783 (2017). doi: 10.1038/s41566-017-0051-x
36. L. Zhu, S. Fan, Persistent Directional Current at Equilibrium in Nonreciprocal Many-Body Near Field Electromagnetic Heat Transfer. *Phys. Rev. Lett.* **117**, 134303 (2016). doi: 10.1103/PhysRevLett.117.134303; pmid: 27715122
37. D. L. C. Chan, M. Soljačić, J. D. Joannopoulos, Direct calculation of thermal emission for three-dimensionally periodic photonic crystal slabs. *Phys. Rev. E* **74**, 036615 (2006). doi: 10.1103/PhysRevE.74.036615; pmid: 17025772
38. This issue is compounded by the sensitivity of the results to assumptions about the spatial and spectral distributions of the dipoles, which are related to the microscopic details of the defect electronic structure, as well as the mechanism of high-energy particle energy transfer into the material.
39. See supplementary materials.
40. H. Demers *et al*., Three-dimensional electron microscopy simulation with the CASINO Monte Carlo software. *Scanning* **33**, 135–146 (2011). doi: 10.1002/sca.20262; pmid: 21769885
41. S. Girard *et al*., Overview of radiation induced point defects in silica-based optical fibers. *Rev. Phys.* **4**, 100032 (2019). doi: 10.1016/j.revip.2019.100032
42. In principle, one would want to compare V_{eff} in the TF to a "truly intrinsic" or "bulk" silica case. In that case, one would compare to silica of the same thickness (1000 nm). However, because this reference case is a thin film as well, nanophotonic shaping effects in the spectrum will inevitably be present. Comparing the V_{eff} in the thin-film case of Fig. 2 to thin films without (i) the top Si layer or (ii) without both Si layers (see fig. S1), one finds that the TF of Fig. 2 presents slightly smaller absorption enhancement at the red peak, possibly due to the high reflectivity of the top Si layer (suppressing the amount of field that can be absorbed by the material). However, the PhC sample still shows strong shaping and enhancement relative to all TF cases.
43. P. Lecoq *et al*., Roadmap toward the 10 ps time-of-flight PET challenge. *Phys. Med. Biol.* **65**, 21RM01 (2020). doi: 10.1088/1361-6560/ab9500; pmid: 32434156
44. E. Yablonovitch, Statistical ray optics. *J. Opt. Soc. Am.* **72**, 899 (1982). doi: 10.1364/JOSA.72.000899
45. P. Campbell, M. A. Green, The limiting efficiency of silicon solar cells under concentrated sunlight. *IEEE Trans. Electron Dev.* **33**, 234–239 (1986). doi: 10.1109/T-ED.1986.22472

46. R. N. Raman, M. J. Matthews, J. J. Adams, S. G. Demos, Monitoring annealing via CO_2 laser heating of defect populations on fused silica surfaces using photoluminescence microscopy. *Opt. Express* **18**, 15207–15215 (2010). doi: 10.1364/OE.18.015207; pmid: 20640006
47. Z. Yu, A. Raman, S. Fan, Fundamental limit of nanophotonic light trapping in solar cells. *Proc. Natl. Acad. Sci. U.S.A.* **107**, 17491–17496 (2010). doi: 10.1073/pnas.1008296107; pmid: 20876131
48. A. I. Zhmakin, Enhancement of light extraction from light emitting diodes. *Phys. Rep.* **498**, 189–241 (2011). doi: 10.1016/j.physrep.2010.11.001
49. S. Derenzo, E. Bourret, C. Frank-Rotsch, S. Hanrahan, M. Garcia-Sciveres, How silicon and boron dopants govern the cryogenic scintillation properties of N-type GaAs. *Nucl. Instrum. Methods Phys. Res. A* **989**, 164957 (2021). doi: 10.1016/j.nima.2020.164957
50. S. Liu *et al*., Light-Emitting Metasurfaces: Simultaneous Control of Spontaneous Emission and Far-Field Radiation. *Nano Lett.* **18**, 6906–6914 (2018). doi: 10.1021/acs.nanolett.8b02808; pmid: 30339762
51. K. M. Schulz, D. Jalas, A. Y. Petrov, M. Eich, Reciprocity approach for calculating the Purcell effect for emission into an open optical system. *Opt. Express* **26**, 19247–19258 (2018). doi: 10.1364/OE.26.019247; pmid: 30114183
52. Y. Sheng *et al*., Čerenkov third-harmonic generation in $\chi^{(2)}$ nonlinear photonic crystal. *Appl. Phys. Lett.* **98**, 241114 (2011). doi: 10.1063/1.3602312
53. S. Zhang *et al*., Calculation of the emission power distribution of microstructured OLEDs using the reciprocity theorem. *Synth. Met.* **205**, 127–133 (2015). doi: 10.1016/j.synthmet.2015.03.035
54. A. C. Overvig, S. A. Mann, A. Alù, Thermal Metasurfaces: Complete Emission Control by Combining Local and Nonlocal Light-Matter Interactions. *Phys. Rev. X* **11**, 021050 (2021). doi: 10.1103/PhysRevX.11.021050
55. S. Molesky *et al*., Inverse design in nanophotonics. *Nat. Photonics* **12**, 659–670 (2018). doi: 10.1038/s41566-018-0246-9
56. A. G. Polimeridis *et al*., Fluctuating volume-current formulation of electromagnetic fluctuations in inhomogeneous media: Incandescence and luminescence in arbitrary geometries. *Phys. Rev. B* **92**, 134202 (2015). doi: 10.1103/PhysRevB.92.134202
57. W. Yao, F. Verdugo, R. E. Christiansen, S. G. Johnson, Trace formulation for photonic inverse design with incoherent sources. arXiv 2111.13046 (2021).
58. R. E. Christiansen, J. Michon, M. Benzaouia, O. Sigmund, S. G. Johnson, Inverse design of nanoparticles for enhanced Raman scattering. *Opt. Express* **28**, 4444–4462 (2020). doi: 10.1364/OE.28.004444; pmid: 32121681
59. K. Watanabe, T. Taniguchi, T. Niiyama, K. Miya, M. Taniguchi, Far-ultraviolet plane-emission handheld device based on hexagonal boron nitride. *Nat. Photonics* **3**, 591–594 (2009). doi: 10.1038/nphoton.2009.167
60. C. Roques-Carmes *et al*., Data for "A framework for scintillation in nanophotonics" (2021); https://github.com/charlesrc/nanoscint.

ACKNOWLEDGMENTS

We thank T. Savas for assistance in fabricating the sample used for electron-beam scintillation; I. Shestakova and O. Philip (Crytur) for helpful discussions on x-ray scintillators; C. Graf vom Hagen, X. Xu, and J. Treadgold (Zeiss) for feedback on micro-CT scanner experiments; R. Sundararaman (Rensselaer Polytechnic Institute) and J. Coulter (Harvard University) for assistance with DFT calculations; and Y. Salamin and S. Pajovic (MIT) for stimulating discussions. **Funding:** This material is based on work supported in part by the US Army Research Laboratory and the US Army Research Office through the Institute for Soldier Nanotechnologies under contract W911NF-18-2-0048. This material is also in part based on work supported by the Air Force Office of Scientific Research under awards FA9550-20-1-0115 and FA9550-21-1-0299. This work was performed in part on the Raith VELION FIB-SEM in the MIT.nano Characterization Facilities (award DMR-2117609) C.R.-C. acknowledges funding from the MathWorks Engineering Fellowship Fund by MathWorks Inc. **Author contributions:** C.R.-C., N.Ri., N.Ro., I.K., and M.S. conceived the original idea; N.Ri. developed the theory with inputs from C.R.-C. and A.G.; C.R.-C. and S.E.K. performed the electron-beam and x-ray experiments; C.R.-C. and N.Ri. analyzed the experimental data and fitted them to the theory; C.R.-C. and S.E.K. built the electron-beam experimental setup with contributions from J.B., A.M., J.S., Y.Ya., I.K., and M.S.; N.Ri. performed energy loss calculations; C.R.-C. performed absorption map calculations; A.G. performed DFT calculations; C.R.-C. wrote code for optimizing nanophotonic scintillators with inputs from N.Ri., Z.L., and S.G.J.; Y.Yu and C.R.-C. fabricated the x-ray scintillation sample; and J.D.J., I.K., S.G.J., and M.S. supervised the project. The manuscript was written by C.R.-C. and N.Ri. with inputs from all authors. **Competing interests:** The authors declare the following potential competing financial interests: C.R.-C., N.Ri., A.G., S.E.K., Y.Ya., Z.L., J.B., N.Ro., J.D.J., I.K., S.G.J., and M.S. are seeking patent protection for ideas in this work (provisional patent application no. 63/178,176). C.R.-C., N.Ri., Z.L., and M.S. are seeking patent protection for ideas in this work (provisional patent application no. 63/257,611). **Data and materials availability:** The data and codes that support the plots within this paper and other findings of this study are available online (*60*).

SUPPLEMENTARY MATERIALS

science.org/doi/10.1126/science.abm9293
Materials and Methods
Supplementary Text
Figs. S1 to S19
Table S1
References (*61*–*82*)

21 October 2021; accepted 22 December 2021
10.1126/science.abm9293

A framework for scintillation in nanophotonics

Charles Roques-CarmesNicholas RiveraAli GhorashiSteven E. KooiYi YangZin LinJustin BerozAviram MassudaJamison SloanNicolas RomeoYang YuJohn D. JoannopoulosIdo KaminerSteven G. JohnsonMarin Solja#i#

Science, 375 (6583), eabm9293. • DOI: 10.1126/science.abm9293

Scintillating nanophotonics

When a high-energy particle collides with a material, the energy is transferred to atoms in the material, and light can be emitted. This scintillation process is used in many detector applications ranging from medical imaging to high-energy particle physics. Roques-Carmes *et al*. integrated scintillating materials with nanophotonic structures to enhance and control their light emission (see the Perspective by Yu and Fan). The authors show how nanophotonic structures enable the ability to shape the spectral, angular, and polarization characteristics of scintillation. This approach should enable the development of brighter, faster, and higher-resolution scintillators. —ISO